

The impacts of environmental variables on water reflectance measured using a lightweight unmanned aerial vehicle (UAV)-based spectrometer system



Chuiqing Zeng*, Murray Richardson, Douglas J. King

Department of Geography and Environmental Studies, Carleton University, 1125 Colonel By. Drive, Ottawa, ON K1S 5B6, Canada

ARTICLE INFO

Article history:

Received 13 April 2017

Received in revised form 17 May 2017

Accepted 8 June 2017

Keywords:

Water reflectance

Environmental variables

Hyperspectral data

Water quality

Chlorophyll-a

Turbidity

CDOM

Unmanned Aerial Vehicle (UAV)

ABSTRACT

Remote sensing methods to study spatial and temporal changes in water quality using satellite or aerial imagery are limited by the inherently low reflectance signal of water across the visible and near infrared spectrum, as well as environmental variables such as surface scattering effects (sun glint), substrate and aquatic vegetation reflectance, and atmospheric effects. This study exploits the low altitude, high-resolution remote sensing capabilities of unmanned aerial vehicle (UAV) platforms to examine the major environmental variables that affect water reflectance acquisition, without the confounding influence of atmospheric effects typical of higher-altitude platforms. After observation and analysis, we found: (1) multiple water spectra measured at the same location had a standard deviation of 10.4%; (2) water spectra changes associated with increasing altitude from 20 m to 100 m were negligible; (3) the difference between mean reflectance at three off-shore locations in an urban water body reached 29.9%; (4) water bottom visibility increased water reflectance by 20.1% in near shore areas compared to deep water spectra in a clear water lake; (5) emergent plants caused the water spectra to shift towards a shape that is characteristic of vegetation, whereas submerged vegetation showed limited effect on water spectra in the studied lake; (6) cloud and sun glint had major effects and caused water spectra to change abruptly; while glint and shadow effects on spectra may balance each other under certain conditions, the water reflectance can also be unpredictable at times due to wave effects and their effects on lines-of-site to calm water; (7) water spectra collected under a variety of different conditions (e.g. multiple locations, waves) resulted in weaker regression models compared to spectra collected under ideal conditions (e.g. single location, no wave), although the resulting model coefficients were relatively stable. The methods and results from this study contribute to better understanding of water reflectance acquisition using remote sensing, and can be applied in UAV-based water quality assessment or to aid in validation of higher altitude imagery.

© 2017 International Society for Photogrammetry and Remote Sensing, Inc. (ISPRS). Published by Elsevier B.V. All rights reserved.

1. Introduction

Water-quality indicators of inland waterbodies such as lakes and rivers are widely used to guide resource management, ensure drinking water safety, protect public health, and control pollution and diseases (Moore et al., 2014). There are, however, limitations on current abilities to characterize spatial and temporal variability of water quality conditions over water bodies, using *in situ* measurement (Dörnhöfer and Oppelt, 2016). Increasingly, researchers are turning towards satellite and airborne remote sensing technol-

ogy (e.g., Olmanson et al., 2013; Brezonik et al., 2015; Matsushita et al., 2015; Mouw et al., 2015) as a complementary tool for generating detailed, spatially and temporally distributed water quality information.

Remote sensing approaches have most commonly been applied to the retrieval of optical water quality parameters of inland water such as Chlorophyll-a (Chl-a), turbidity, and coloured dissolved organic matter (CDOM) (Odermatt et al., 2012; Matsushita et al., 2015; Watanabe et al., 2016), and others (Chen et al., 2014; Knudby et al., 2016; Song et al., 2017). Most studies have used empirical regression models between water reflectance in different spectral bands and water quality parameters; such models are often valid only in the studied water bodies. A detailed summary

* Corresponding author.

E-mail addresses: Chuiqing.Zeng@carleton.ca (C. Zeng), Murray.Richardson@carleton.ca (M. Richardson), Doug.King@carleton.ca (D.J. King).

and comparison of different empirical methods was given in Matthews (2011) and Dörnhöfer and Oppelt (2016). In contrast to empirical models, bio-optical models utilize bio-geophysical attributes of water based on radiative transfer equations. These physically-based approaches are potentially more effective for modelling water quality, particularly since they are, theoretically, more generalizable and therefore transferable in space and time. Detailed reviews of physics-based inversion methods can be found, such as Odermatt et al. (2012), Palmer et al. (2015), and Dörnhöfer and Oppelt (2016).

To better understand water spectral characteristics, hyperspectral imagery has been used to investigate water-light interactions and retrieval of water-quality parameters for more than two decades (e.g., Vasilkov and Kopelevich, 1982; Vertucci and Likens, 1989; Lee et al., 1999; Zarco-Tejada et al., 2012). Hyperspectral data are comprised of tens to hundreds of spectral bands usually with 1–10 nm spectral resolution. This high spectral resolution can enhance capabilities to distinguish water reflectance changes caused by inherent optical properties of water. For example, Wang et al. (2016) estimated Chl-a concentrations in fresh water outdoor ponds in south China based on surface reflectance derived from laboratory spectra, using an empirical model. Satellite sensors, however, remain limited in their ability to collect imagery with high spatial, spectral, and temporal resolution. Airborne sensors (e.g., Bergamino et al., 2010; Olmanson et al., 2013) are currently the major source of hyperspectral imagery suitable for inland water-quality research, but they can be prohibitively expensive and time-consuming with respect to flight planning and implementation.

Apart from hyperspectral data scarcity, water is unique from other ground features for its low reflectance in visible and near-infrared wavelengths. Less than 10% of the radiation of water pixels received at the satellite sensor originates directly from the water column (Giardino and Kondratyev, 1991), while over 90% of the remaining signal is from water surface, the atmosphere (Moore et al., 1999), and adjacent pixels (Santer and Schmechtig, 2000). Therefore, decomposing satellite image radiation to retrieve actual reflectance from inland water is challenging yet critical for water constituent concentration modelling. Furthermore interactions between light and water include scattering, absorption, and attenuation, and these are affected by environmental variables such as waves on the water surface, particles or vegetation in the water and, in the case of shallow waters, the bottom substrate (Mobley, 1999). It is therefore difficult to separately analyze these environmental variables and their effects on water quality parameter estimation. The light-water interaction is usually studied via simulating water quality parameters (Gallegos, 2001; Lee et al., 2005; McKee et al., 2007) or laboratory experiments (Zhang et al., 2009; Wang et al., 2016), but natural light and natural environmental conditions differ from simulations and lab experiments. Hence a platform without atmosphere effects and that offers more control over environmental variables during data acquisition is valuable for studying water-light interactions and further water constituent modelling.

Unmanned aerial vehicles (UAV) are a rapidly evolving, affordable, and flexible remote sensing platform that provide exceptional control over the flight location, time, altitude, path, and angle. With hyperspectral sensors mounted on low-altitude UAV platforms, data can be collected with negligible atmospheric effect and high spatial resolution. The improvement of UAV platforms and the miniaturization of sensors have stimulated much remote sensing research and development of new systems (Colomina and Molina, 2014; Pajares, 2015). Specifically in the hyperspectral domain, there are new sensor system developments (Uto et al., 2016), data calibration using field or lab spectrometry (Liu et al., 2014; Aasen et al., 2015), and inversion models for the study of

water quality parameters (Ampe et al., 2015). Currently, two dimensional (2D) hyperspectral imaging systems are generally too heavy and/or complex to operate on small low cost UAVs. Moreover, most hyperspectral imagers rely on accurate GPS/IMU instrumentation and an on-board computer for effective data collection. Finally, hyperspectral cameras are expensive, adding an additional financial liability, particularly for UAV applications over water where aircraft failure would almost certainly result in complete loss of the imaging system. The objectives of this study, therefore, were threefold: (1) to develop a system to acquire 1D spectra for small water bodies using a light-weight, low-cost spectrometer mounted on a consumer-grade UAV platform; (2) to study the impact of internal (i.e., sensor stability, noise floor) and environmental (i.e., location, altitude, illumination conditions) variables on water spectra, and (3) to build preliminary water quality regression models using acquired spectra, and analyze the impact of environmental variables on such models.

2. Materials and Methods: UAV system design and data processing

2.1. UAV spectrometer system components and reflectance measurement

The data collection system is designed for consumer-level UAVs in order to minimize cost and to promote flexibility and ease-of-use. Fig. 1 shows the air and ground units of the system. The air unit is comprised of a UAV platform and associated components, including the navigation and flight control systems, a standard color (RGB) camera and a compact spectrometer. The micro-computer in the air unit communicates with the sensor control system via wireless network to start, stop, and view the spectrometer data during UAV flights within the range of the wireless signal. The color camera collects videos and images to help with interpretation of spectral data, in particular the assessment of water surface conditions associated with wind and sun. The spectrometer and the color camera are mounted under the UAV and visually aligned to nadir view. Data collected by these two sensors are matched over time by their time stamp with 1 s resolution.

In this study we used two UAV platforms, a quad-copter (DJI Phantom 2 Vision Plus) and a hexa-copter (DJI Spreading Wings S800). The quad-copter and the hex-copter have take-off weights (including the sensors) of 1.4 kg and 6 kg, respectively. Since small multi-rotor aircraft are now widely available, a detailed description of these specific models is not presented. The spectrometer (Ocean Optics STS-VIS) is 4.0 cm × 4.2 cm × 2.4 cm and weighs 60 g. It has a spectral range from 350 nm to 800 nm with 1.5 nm optical spectral resolution, and 1024 spectral bands in this wavelength range. The field of view (FOV) is 25°, which produces a footprint of approximate 44.3 m diameter at an altitude of 100 m. The integration time is manually set between 100 ms and 1000 ms, depending on illumination conditions. The spectrometer is controlled by a Raspberry PI 3 Model B microcomputer (dimensions with case: 22.9 cm × 17.5 cm × 4.8 cm), which is remotely operated through a 2.4 GHz wireless network. A 3000 mAh lithium ion battery is used, which lasts about 3.0 h in operation. In total, the air unit spectrometer components weigh approximately 190 g. Spectrometer dark noise sensitivity to temperature and the comparison of spectrometer reflectance over reference targets were discussed in Appendix A.

The ground unit includes the flight control system, the sensor control system, and a second STS-VIS spectrometer pointed vertically upward to record downwelling sun and sky radiance. The flight control system has a transmitter and a mobile device such as a tablet, a smartphone, or a laptop to design flight paths and

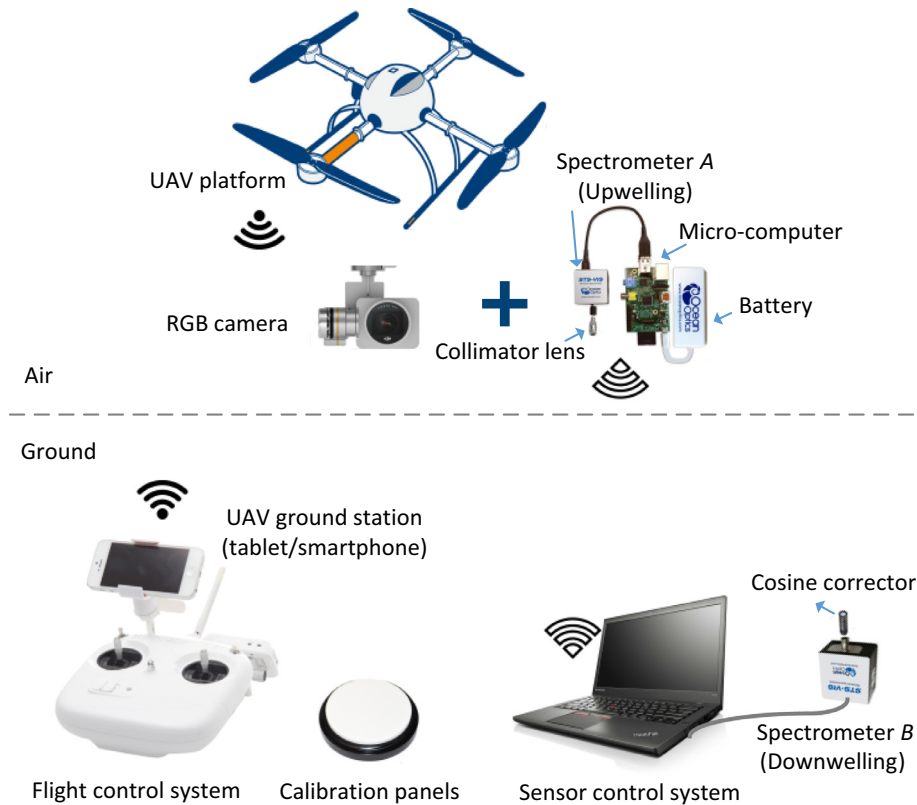


Fig. 1. UAV spectrometer system.

operate the drone. On the ground, the second spectrometer is attached with a cosine corrector which collects radiance in a 180° FOV and is pointed upwards to monitor illumination conditions. A laptop is used to communicate with both spectrometers, in the air and on the ground, to setup the spectrometer parameters such as integration time and acquisition timing before a flight. A reference panel is measured by the spectrometer in the air unit before and after each flight to calibrate the spectrometers and calculate water reflectance.

The flight control software is the DJI Go App for quad-copter and the GroundStation 4.0 software for the hexa-copter, both of which provide real time monitoring of the drone status such as flight speed, altitude, and battery status. The DJI Go App also controls the color camera on the quad-copter to view real time video and adjust the view angle. The hexa-copter is operated in autopilot mode with pre-defined waypoints. The quad-copter is operated in manual flight mode, using a pre-loaded map to show the flight path in real time, and to view or save waypoints. The spectrometer is operated through a web-page where integration time and other acquisition parameters are set. Although this spectrometer could also be mounted on the UAV, placing it on the ground near the site captures the same illumination information while minimizing the weight of the air unit. A white barium sulphate reference disc (ASD Spectralon, 9.2 cm diameter, U.S. Pharmacopeial Convention (USP) for USP 1119) is used in this study.

Target reflectance was calculated as follows:

$$\rho'(\lambda) = \frac{I(W, \lambda) - I(D, \lambda)}{I(R, \lambda) - I(D, \lambda)} \quad (1)$$

where ρ' is the nominal surface reflectance, λ is wavelength, I is the radiant intensity measured by the spectrometer sensor (in arbitrary units) for the water surface (W), white reference (R) and dark signal (D). The dark signal represents internal sensor noise and was measured with the lens cap on. To obtain the actual reference ρ , nomi-

nal reflectance ρ' is adjusted based on illumination conditions measured by the ground spectrometer:

$$\rho(\lambda) = \rho'(\lambda) \times \frac{E(W)}{E(R)} = \rho'(\lambda) \times \frac{\int [E(W, \lambda) - E(D, \lambda)] d\lambda}{\int [E(R, \lambda) - E(D, \lambda)] d\lambda} \quad (2)$$

where E is the downwelling irradiance (Mobley, 1994) measured by the ground spectrometer. $E(W)$ and $E(R)$ are measured coincidentally with $I(W)$ and $I(R)$. The integral of irradiance, after subtracting the dark signal, $E(D, \lambda)$, over all wavelengths is employed to represent the total sun intensity at a given time.

2.2. Investigation of water spectra variation under various environments

2.2.1. Data collection for water bodies

Fourteen different water bodies were included in this study. At each water body, UAV flights were conducted to cover multiple locations and multiple altitudes. Sampling locations occurred along a pre-defined route from the shoreline to the center of the water body and back, with altitudes normally ranging between 20 m to 100 m to evaluate the effects of altitude on the recorded spectra. Based on site accessibility at lake shores or river banks, UAV flight paths were designed on a case by case basis, trying to reach the center of a water body when it was safe. Atmospheric effects at these altitudes were deemed to be negligible. Sun zenith angle was always between 22.0° and 45.1° during the period of data collection and flights, so specular reflectance was not present within the 25° FOV of the spectrometer when flat water was observed from nadir view. Fig. 2 shows a typical flight path and water reflectance data acquisition at three different locations and two altitudes.

Water samples were collected in 4L HDPE bottles at the water surface approximately 2 m from the shore to represent a flight area. For natural lakes without significant inflows that can cause

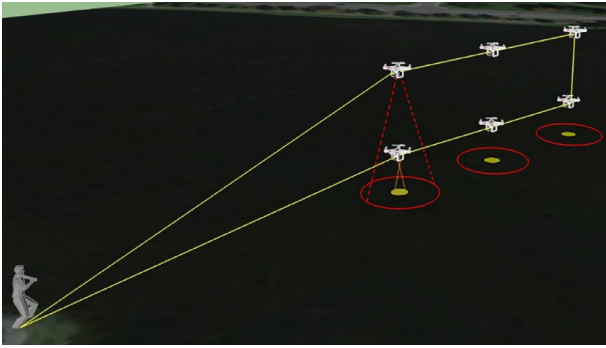


Fig. 2. A typical UAV flight path over water. The spectrometer footprints associated with the two altitudes (20 m and 100 m) are shown as yellow and red circles.

water quality to vary spatially, water quality parameters and associated spectral curves over small geographic areas are known to not vary significantly (Wang et al., 2006; Shuhaimi-Othman et al., 2007; Binding et al., 2015). Samples were returned to a laboratory and processed the same day or stored in a refrigerator to be processed the following day. A RBRmaestro multi-parameter water quality sonde (RBR Ltd.) was used to measure Chl-a, conductivity, CDOM, pH, etc. A DR/890 colorimeter was used to measure turbidity, and a Cary60 UVvis spectrophotometer to measure absorbance. Chlorophyll-a and CDOM concentrations were derived using Turner Designs Cyclops-7 submersible sensors attached to the RBRmaestro with minimum detection limits of 0.3 $\mu\text{g/L}$ and 0.5 ppb, respectively. To minimize the variability among samples, for the water constituent measurements, samples were fully shaken then measurements were taken for five consecutive minutes. The truncated mean (Barr and Sherrill, 1999) was calculated after removing the lowest and highest 20% of sample values, in order to avoid measurement outliers.

2.2.2. Assessment of water spectra

A UAV-based spectral reflectance measurement system can be used to survey water bodies at various locations, altitudes, and view angles, with repeated measurements over the same location to minimize the impact of spectra variations. Water reflectance spectra were assessed for variability at a given location by hovering the UAV over that location, at different locations within a given water body and at different altitudes between 20 m and 100 m over the same location to test the effect of footprint size. The effects on reflectance of cloud and sun glint (due to surface waves), water depth, and aquatic plants are also evaluated. Assisted by video imagery, images within spectrometer footprints were classified into different surface condition types (glint, calm water, shadow, and the rest that could not be confidently classified into any of the three categories) to analyze the corresponding changes of water reflectance.

2.2.3. The impact of environmental variables on water parameter modelling

To assess potential for water quality parameter estimation using the acquired high spectral and spatial resolution data, two-band ratios were employed in linear regression models. UAV sensors are frequently dis-assembled and re-assembled for different flights and for transportation. It is time consuming and expensive to calibrate UAV sensors for absolute radiance measurement but relative calibrated with a white reference panel is easier. Hence a two-band ratio approach was applied to mitigating the uncertainty of calibration. The ratios were derived from averaged spectra for each of the 14 lakes. Many band ratios for water quality parameter estimation have been proposed or reviewed in the literature such

as (Matthews, 2011; Odermatt et al., 2012; Palmer et al., 2015). Instead of testing a specific set of these, all possible 2-band ratios were tested sequentially to determine those that produced the best linear regression models for the water parameters of Chl-a, CDOM, and turbidity.

Given the total field sample size was small (one water sample per lake given high within-lake spatial auto-correlation), leave-one-out cross validation (Cristianini et al., 2004) was applied for model validation. Two groups of regression models for water quality parameters were compared and analyzed, including models constructed with; (1) only water spectra collected under ideal conditions (calm, deep water); and (2) all water spectra, including those collected under ideal and non-ideal conditions (with wave and glint effects). The purpose of the second group of models was to determine the sensitivity of the models' goodness-of-fit and regression parameters to water surface conditions.

3. The impact of environmental variables on water reflectance

In this and the following sections, statistical measures are used to quantitatively compare the spectra within a lake and between lakes. These *metrics* include the MEAN, standard deviation (STD), mean absolute difference (MD), and standard error of the mean (SEM). Spectra *variables* are original reflectance (R), the mean reflectance (M), or the percent reflectance relative to mean reflectance (PER). For example, STD(PER) describes the standard deviation of percent reflectance relative to its mean reflectance of the spectra.

3.1. Variability in repeated spectral measurements at a single location

With a set of 103 spectra taken at the same location during a period of 24 s over a lake, the original and averaged samples are shown in Fig. 3. A mean filter with window size of 11 bands (about 5.06 nm) was applied to each spectrum to produce a smooth curve. Each spectrum is noisy, especially at low and high wavelengths, while the average spectrum is largely improved. Reflectance for bands above 700 nm was sometimes slightly below zero when the dark signal intensity was greater than the water intensity according to Eq. (1). The average standard deviation of the percent reflectance to the mean reflectance for the 103 spectra, STD(PER), is 10.3%. The corresponding STD(R) is 0.00076 and the MEAN(R) is 0.0073 (or 0.73%).

Reflectance ranges from 0.0088 to 0.0108, in Fig. 3. This reflectance range of 0.002, despite being small in absolute terms, is about 20% of the Mean reflectance of 0.0097. 20% is a significant proportion of the total signal. Together with the STD(PER), this figure illustrates the need to average spectra at a given sample location rather than using any single spectrum.

3.2. Water spectra for different locations within a given water body

Fig. 4 shows the comparison of water spectra at different locations of the same water body. The average spectrum at each location was calculated according to the method shown in Fig. 3. Dow's Lake is a constructed urban lake and the three locations measured in Fig. 2 show different spectra, with the STD(PER) of 3.2%, 6.0%, and 2.2%, respectively, and SEM(PER) of 0.47%, 0.66%, and 0.30%, respectively, over the 400–800 nm range for the three locations. The mean absolute differences of these averaged spectra between pairs of locations (i, j), $MD(M_i, M_j)$, were: 0.0045 (Loc 1–2), 0.0034 (Loc 1–3), and 0.0011 (Loc 2–3). In relative terms, these differences are 29.9%, 22.6%, and 7.1%, respectively, of their approximate spectra maximum (1.5%) in (d). Although acquired sequentially, measurements at the three locations inevitably have

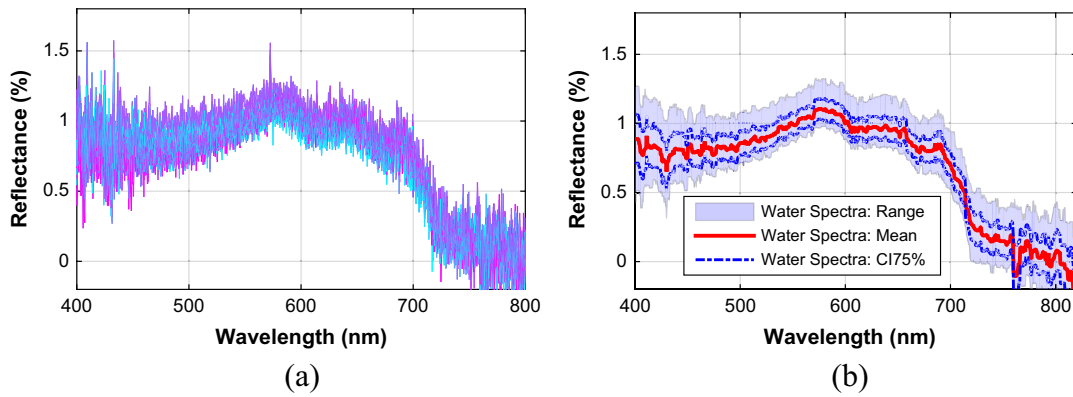


Fig. 3. An example of spectra measured at Lac Leamy on May 30th, 2016. (a) 103 spectra with gradual color change according to the acquisition time sequence, and (b) the corresponding data range (shaded), the average spectrum (red line), and the 75% confidence interval (CI) bounds (blue lines). (For interpretation of the references to color in this figure legend, the reader is referred to the web version of this article.)

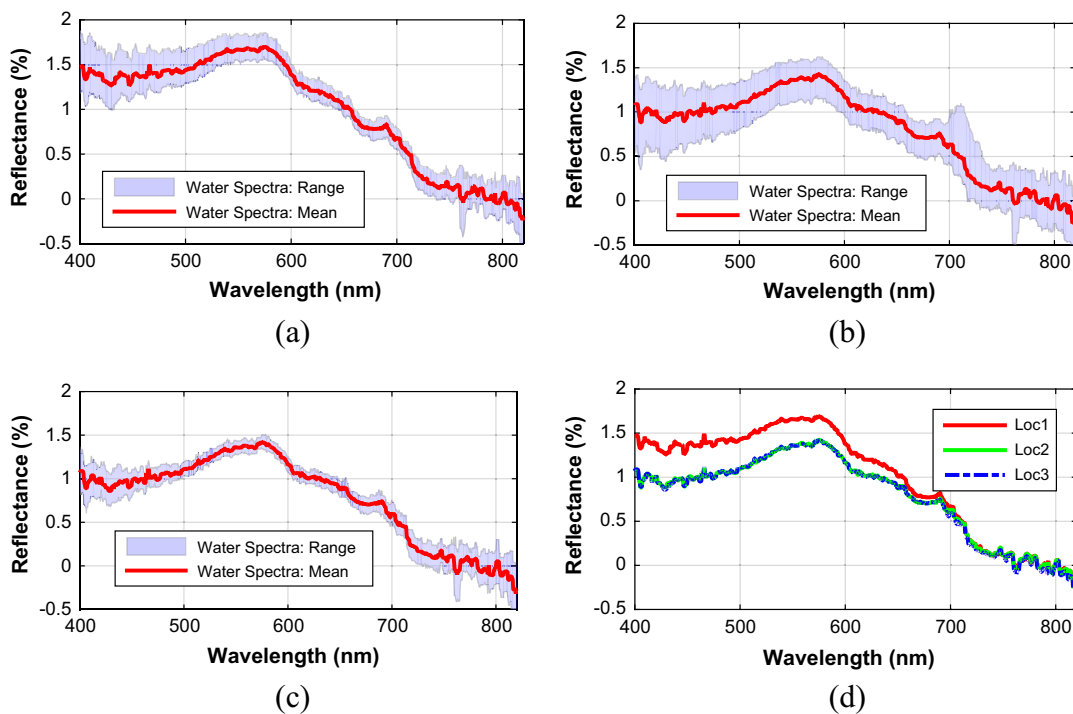


Fig. 4. Example spectra measured at multiple locations over the same water body (Dow's Lake, Ottawa, May 30th, 2016) from an altitude of 20 m. (a–c) are three locations (Loc 1, 2, 3) about 20 m from each other on a flight line, similar to the representation shown in Fig. 2. (d) The average spectra at each of the three locations.

slightly different illumination conditions, which may affect their reflectance. The difference between locations 2 and 3 (7.1%) corroborates our expectation that water spectra do not change significantly in a small area. Loc 1 is closer to the lake shore and was different from Loc 2 and 3, possibly caused by shallower water or sun condition change.

3.3. Water spectra for different altitudes at the same location

Fig. 5(a) and (b) shows RGB camera images of a sample location over Lac Fortune that were taken from 100 m and 20 m altitude, respectively. Fig. 5(c) shows that spectral reflectance variations for measurements taken at several altitudes were not greater than what was found for repeated measurements at 20 m altitude (Fig. 5d). For the data acquired at both altitudes and the repeated data acquired at one altitude, STD(PER) was 2.9% and 6.4% and SEM(PER) was 0.26 and 1.72, respectively. Theoretically, radiance

at a sensor is independent of altitude, given atmospheric effects are negligible, and this appears to be true for the range of altitude tested here. Minor exceptions to this are shown in Fig. 5(c) where the highest altitude corresponded to slightly higher reflectance in the ultraviolet-violet and near-infrared than the reflectance for the lower altitudes.

3.4. Effects of water depth on water spectra

In a series of measurements from deep water toward the lake shore at an altitude of 10 m, 32 water spectra were collected. Every second measurement ($n = 16$) was analyzed. Fig. 6(a–c) shows RGB camera images of the first, middle, and last measurement locations (Scenes 1, 8, and 16) and their corresponding spectrometer footprints. The spectra corresponding to these 16 locations are shown in Fig. 6(d). The lake bottom is not visible in the spectrometer footprint of scene #1, while in scene #16, where water depth is less

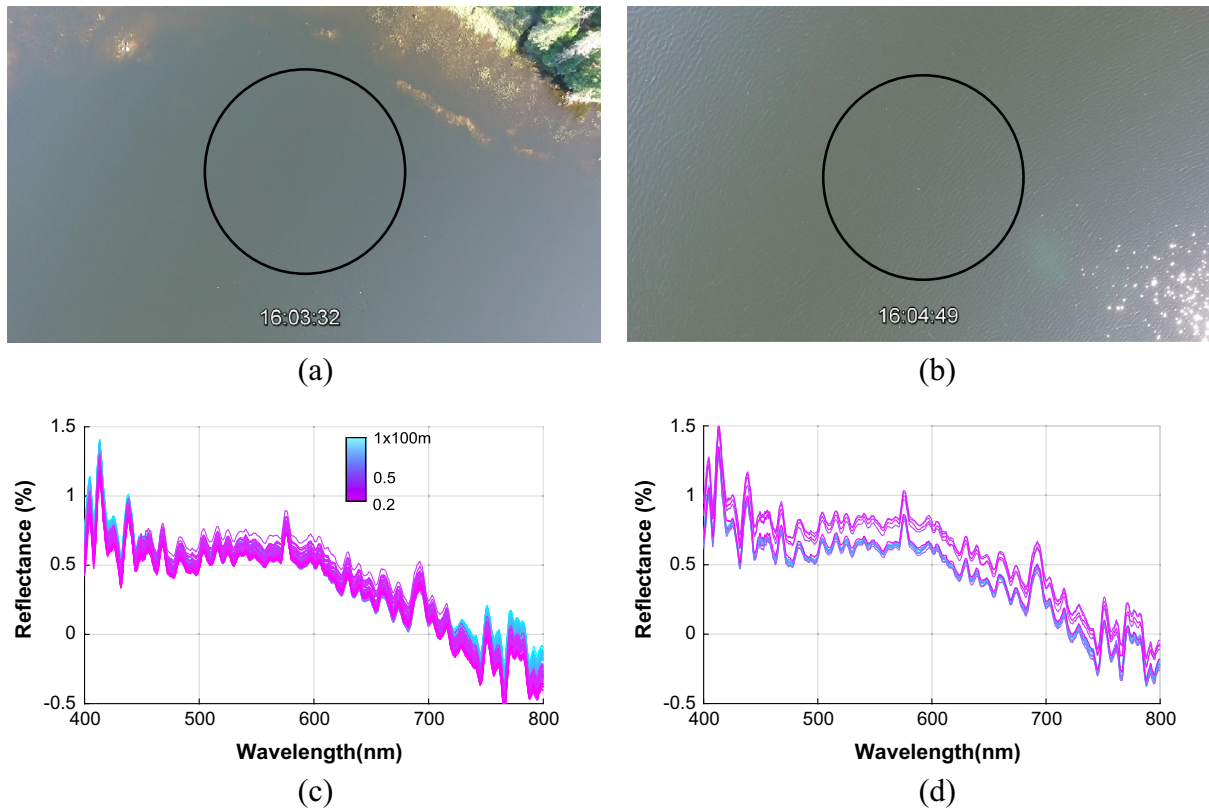


Fig. 5. Water spectra variations with altitude, Lac Fortune, September 20th, 2016. (a, b) RGB images from 100 m and 20 m altitude, respectively. The spectrometer footprint is shown as a circle in each photo (8.86 m at 20 m altitude). (c) Water spectra for 14 samples at different altitudes between 20 m and 100 m. (d) Water spectra from repeated measurements at 20 m altitude at a single location. The variation in spectra from such repeated measurements (d) was equal to or greater than the variation in spectra with varying altitude and footprint size (c).

than 0.5 m, rocks and logs are clearly visible. Fig. 6(d) shows that water reflectance at most bands steadily increased from deep to shallow conditions, due to the increasing reflectance from the lake bottom. The average relative increase in reflectance from scene #1 to scene #16, $MD(\#1, \#16)/R(\#1)$, was 20.1%.

3.5. Effects of aquatic vegetation on water spectra

Emergent, surface and below surface vegetation also affects water reflectance spectra. Fig. 7(a) shows no visible reflectance from vegetation and therefore has low overall reflectance as shown in Fig. 7(d). Fig. 7(b) and (c) show visible below surface and emergent vegetation, respectively. The below surface vegetation surprisingly has little effect on water reflectance while the emergent plants increase overall reflectance and produce spectra that are similar to healthy vegetation (Fig. 7d).

3.6. Effects of sun glint on water spectra

To understand the effects of cloud and wave generated sun glint on the UAV spectra, continuous measurements were made over a lake under a variety of sky and wave conditions. Each water spectrum was measured from 20 m altitude within the 25° FOV (8.86 m diameter footprint). Three such conditions and measurements are provided in Fig. 8 to illustrate the main findings. In all cases, the radiance from the white reference disc was measured prior to the flight under sunny conditions. Scene #1 (Fig. 8a) represents the best conditions of the three scenes with no discernable waves or sun glint and only a small portion of the footprint showing reflectance from an overhead cloud. Its reflectance values were

the lowest of the three conditions. Scene #2 (Fig. 8b) had distinct cloud reflectance in about 60–70% of the footprint. Such reflected radiance from the water surface increases the overall water reflectance as shown in Fig. 8d. Scene #3 (Fig. 8c) shows distinct sun glint and this contributed to the highest overall reflectance and variation in spectra as seen in Fig. 8d. Sun glint increases the reflectance in all bands, but the magnitude of the increase is dependent on the wave size and shape. For these three scenes, as the amount of glint increased from scenes #1 to #3, so did the variation in the spectra (STD(PER) = 2.8%, 4.1%, 9.2%; SEM(PER) at 0.8%, 1.3%, 2.7%, respectively).

3.7. Analysis of water spectra components within the spectrometer footprint

Video imagery was recorded concurrent with spectrometer measurements. The size and location of the spectrometer footprints within a given image were determined by the geometry and FOV of the video camera and the spectrometer. One water spectrum per second was analyzed with its corresponding footprint scene for a total of 84 spectra-scene pairs. For each water spectra sample, the corresponding footprint within the color image was classified using ISODATA clustering (Ball and Hall, 1965) as illustrated in Fig. 9. Clusters were then manually assigned to meaningful classes: glint, shadow, water, and other. “Glint” is the obvious bright pixels of specular reflection, “Shadow” is the dark side of the waves, “Water” is the calm water pixel area without waves or clouds, and “Other” represents the remaining areas that could not confidently be classified into any of the three categories, comprised mostly of gentle waves that did not belong to one of the above

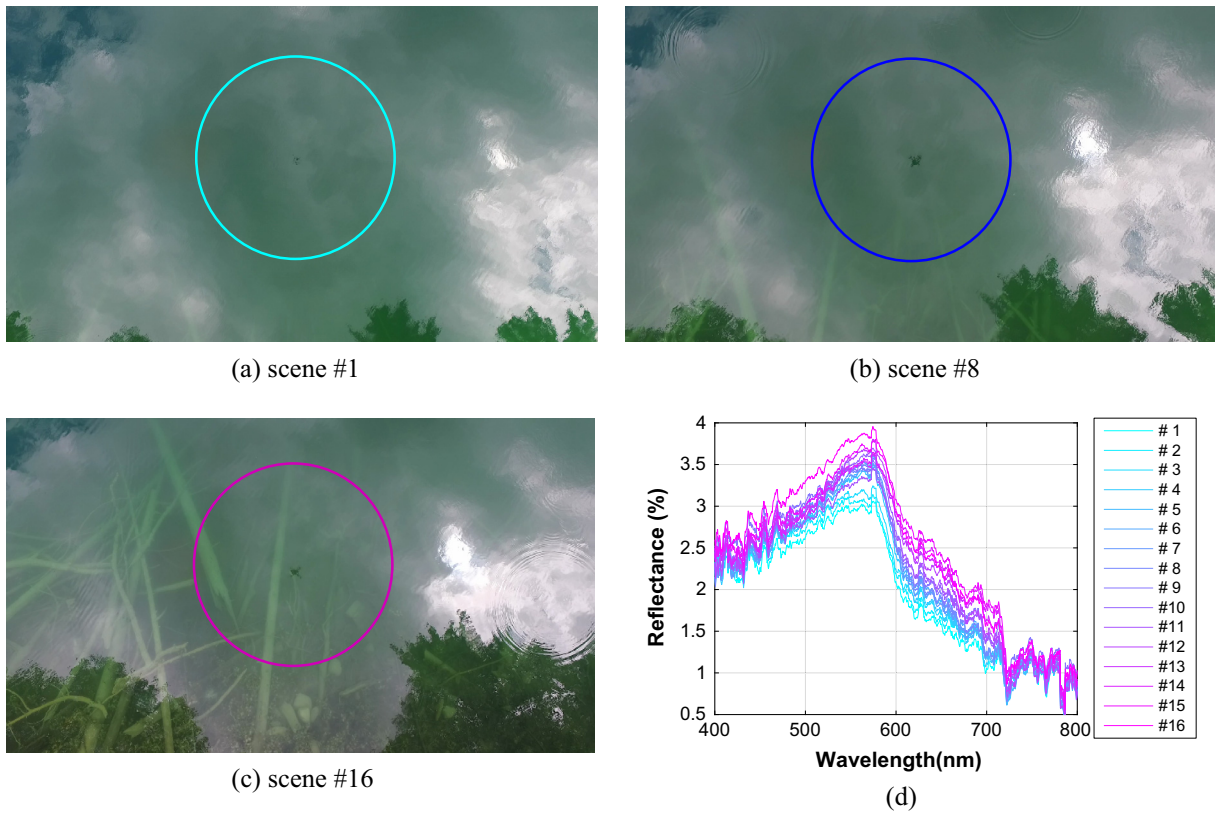


Fig. 6. Spectra variation with water depth and bottom visibility, measured at Pink Lake on July 15th, 2016. (d) shows 16 water spectra; included in these are the spectra for scenes 1, 8, and 16, represented in (a–c).

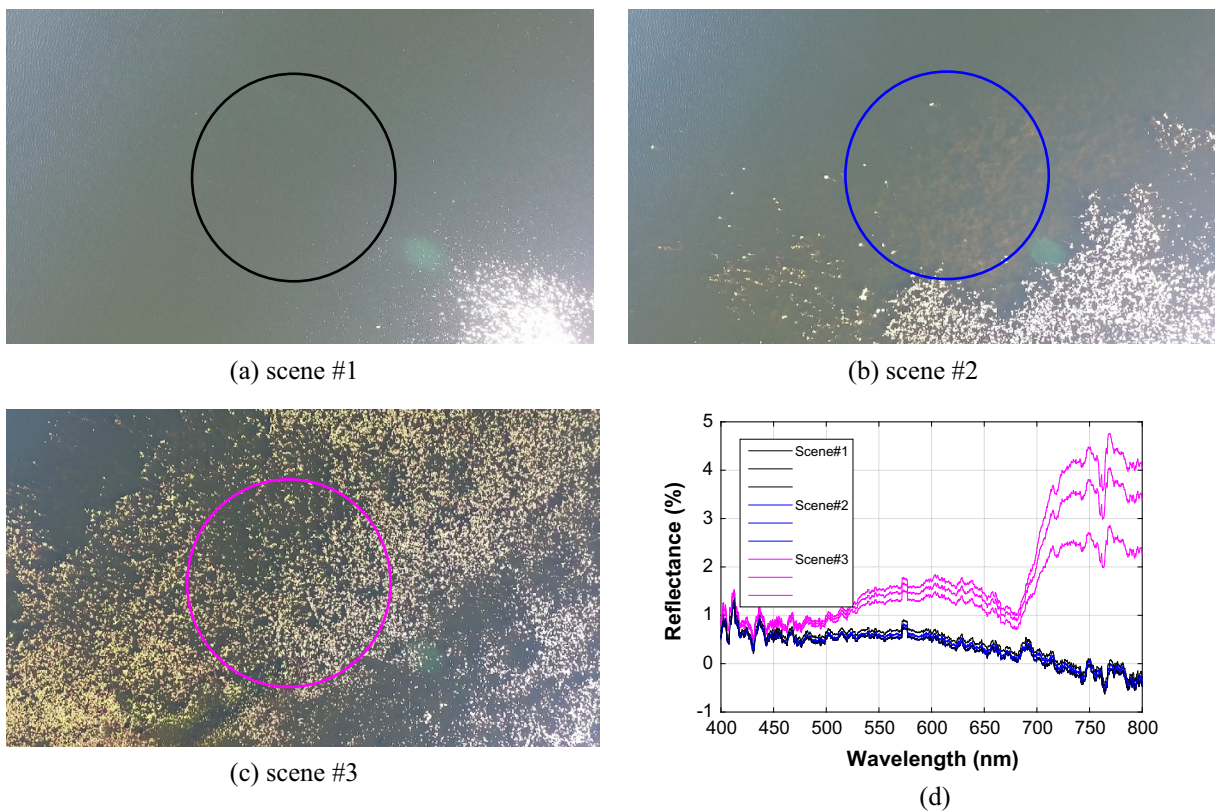


Fig. 7. Water reflectance measurements near the shore of Lac Fortune on September 20th at the same altitude. (a–c) are RGB camera images showing no vegetation, below surface vegetation and emergent vegetation, respectively. Their corresponding spectra are given in (d).

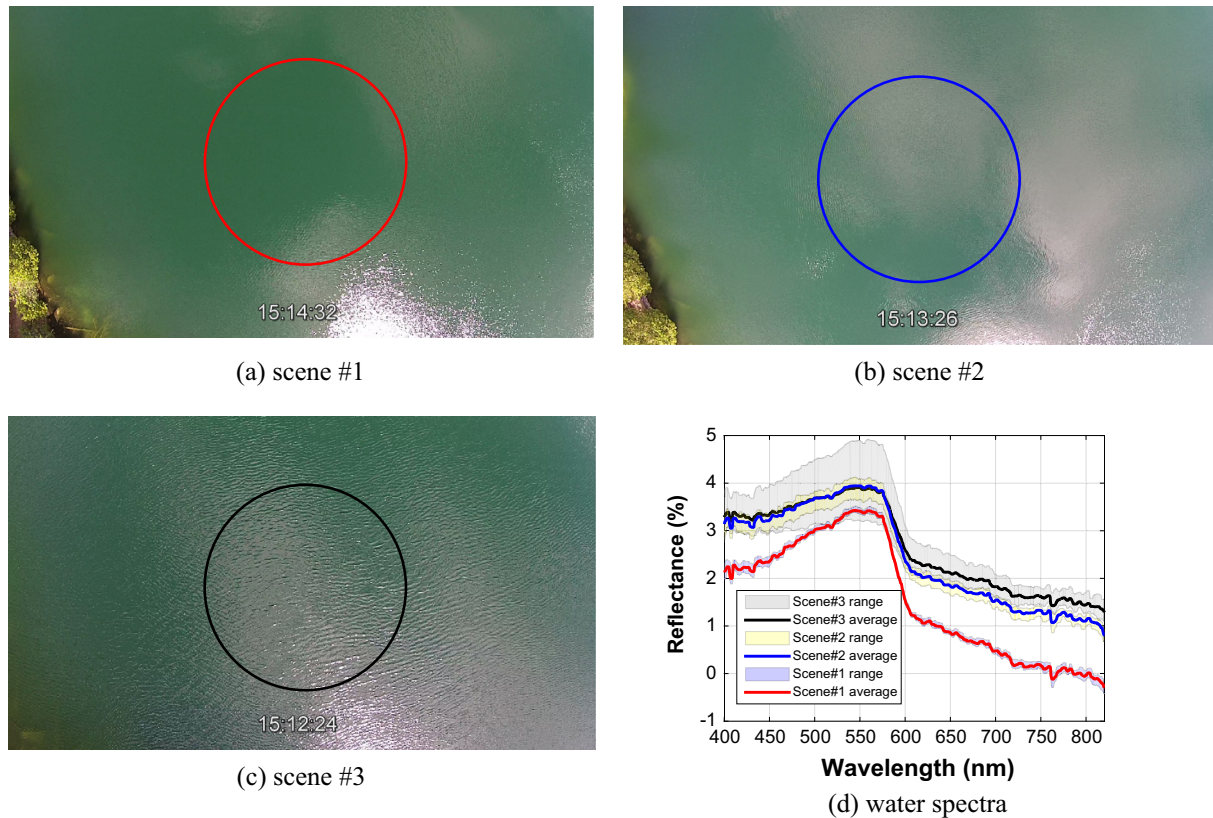


Fig. 8. RGB camera images showing three spectral measurement conditions on Pink Lake on May 30th, 2016 (a–c). (a) a calm water surface under clear sunny condition; (b) partially cloudy weather; (c) waves and glint over water surface. These scenes and measurements were taken about one minute apart with consistent altitude. (d) The corresponding water reflectance range and average spectra.

classes. An example footprint in a color image that mainly consists of glint and shadow is shown in Fig. 9(a), while calm water occupies most of the footprint in Fig. 9(c).

A summary of the scene components of water spectra footprints is shown in Fig. 10. On the x-axis are 81 spectra taken in 2 min over the site used in Fig. 8, from significant shadow and glint (left side of graph) to calm water (right side of graph). Reflectance values at 450 nm, 550 nm, 650 nm, and 750 nm are also plotted. According to this figure, the impact of glint and shadow on water reflectance was complicated and cannot be easily generalized. For example, reflectance was not abnormally high from samples 5 through 20 when glint was high. It also decreased at sample 30 when glint increased. At sample 64, glint increased and seemingly caused an abrupt increase in reflectance. However the proportion of calm water simultaneously increased and remained high for the duration of the experiment, along with reflectance. The highest reflectance (41.8% over average for R550) was recorded for samples 47–48, which had a very small proportion of glint (0.04–0.23%) that is imperceptible in the figure. There are various possible reasons for the complicated effects of glint on water reflectance. Shadows usually coexist with glint (although as shown in Fig. 9, glint comprised a much smaller area than shadow within the footprint) and they likely cancel out each other's effect on water spectra. Waves also change the line of sight from sun to water to sensor, where slight incident angle changes at the water surface can lead to very large water reflectance changes on the order of tens to hundreds of times (Gleason et al., 2012) due to the water surface bi-directional reflectance distribution function. Thus, overall the contribution of sun glint and shadow to average reflectance within a given spectrometer footprint is not easily predicted. In Section 4.2, we examine the implications of these and other environmental variables on regression-based water quality modelling.

4. The impact of environmental variables on water quality models

4.1. Application of the system in water quality modelling

Fig. 11 shows the average spectra for the 14 water bodies after simplifying/filtering. Water quality parameters for these water bodies are listed in Table 1 using the procedure described in Section 2.2.1. The regression results in Fig. 12–14 demonstrate strong linear correlations between the selected spectral water quality indicators and the water parameter measurements ($R^2 = 0.87, 0.61, \text{ and } 0.73$ for Chl-a, CDOM, and turbidity, respectively). Leave-one-out cross validation resulted in an average RMSE of 2.83 $\mu\text{g/l}$ for Chl-a, 3.84 ppb for CDOM, 4.04 FAU for Turbidity. Mean error and mean absolute error were 0.08 and 2.35 $\mu\text{g/l}$ for Chl-a, 0.06 and 2.77 ppb for CDOM, -0.31 and 3.45 FAU for turbidity, respectively. Mean error is close to zero, indicating the models have no or very little bias. The corresponding R^2 for the cross validation, derived from the list of measured water parameters and estimated ones after cross validation, was 0.83, 0.53, 0.60, for Chl-a, CDOM, and Turbidity, respectively. The R^2 reported in cross validation was consistent with that of the regression models in Figs. 6–8. The optimal two-band ratios were consistent with those presented in previous studies. For example, Matsushita et al. (2015) used 665 nm/709 nm, while for our data an optimal ratio was found to be 665 nm/684 nm.

4.2. The impact of environmental variables on water quality parameter modelling

To further study the impact of environmental variables in water quality modelling, we compared the regression models using ideal-

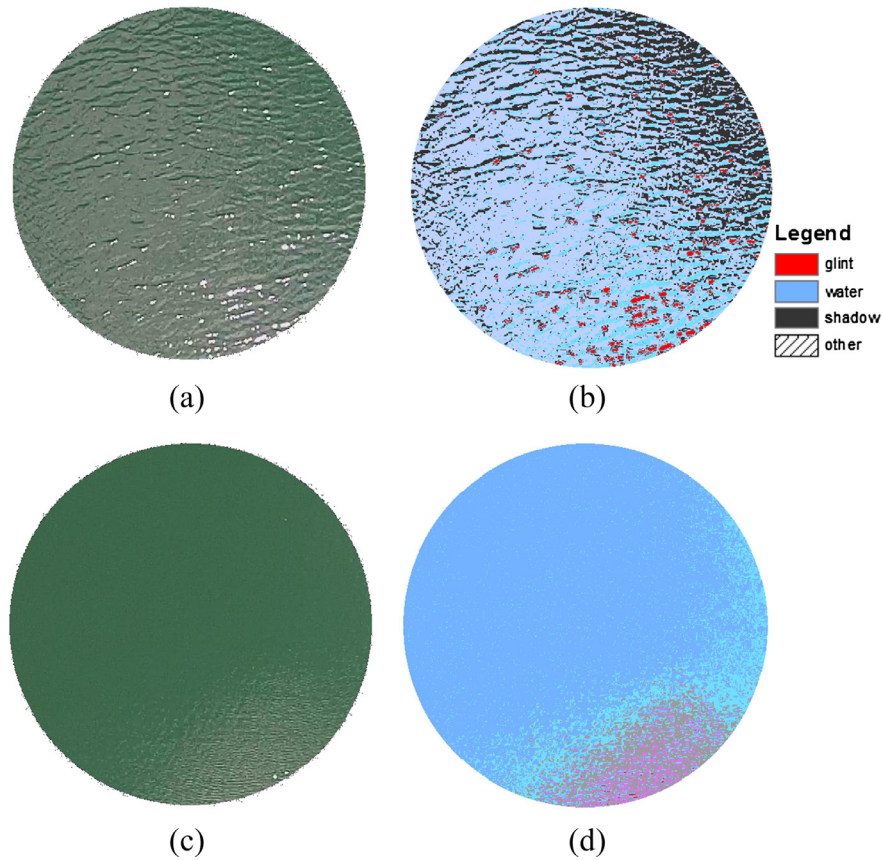


Fig. 9. Examples of color imagery within the spectrometer footprint and their classification, at Pink Lake on May 30th, 2016 (altitude was 20 m; footprint was 8.86 m diameter). (a and b): corresponding to Scene #3 (at 15:12:24) in Fig. 8 with regular color image and classification; (c and d): corresponding to Scene #1 (at 15:14:32) in Fig. 8 with regular color image and classification. Note: because the “Other” includes multiple classes that do not belong to any of the three classes, many classes and colors exist in “Other” and no consistent legend is provided.

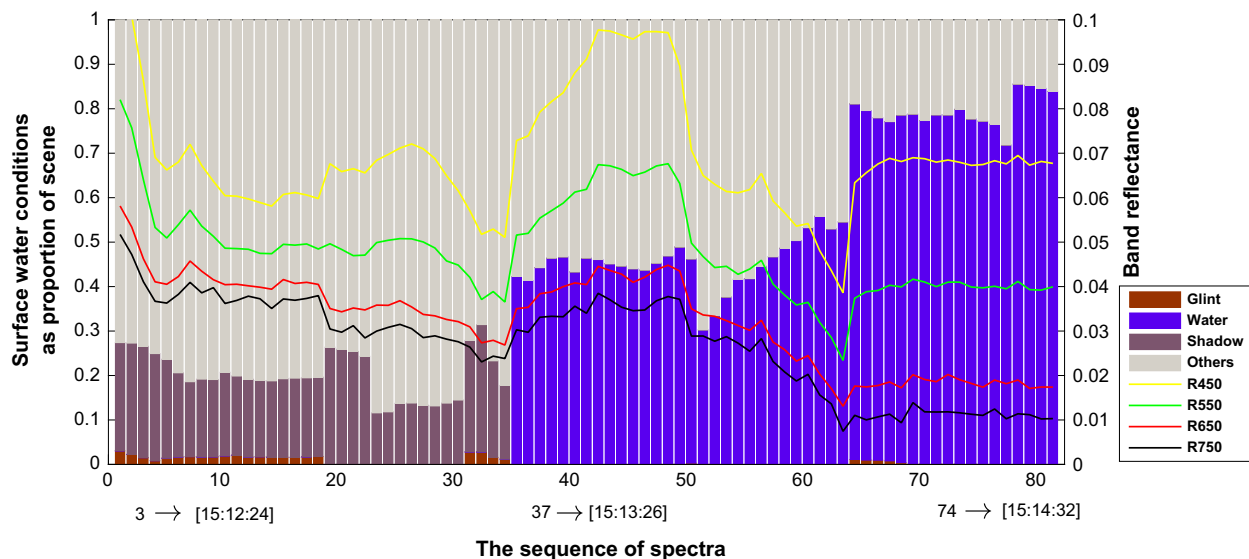


Fig. 10. The distribution of scene components within spectra footprints and the corresponding reflectance at selected wavelengths. The x-axis shows the classified scene components for 81 spectra along a flight transect. The proportion of each scene component within the footprint is shown on the left y-axis. Reflectance for the selected wavelengths is shown on right y-axis. R450 is the reflectance at 450 nm; same for the other curves.

condition water spectra (listed in Fig. 11) and models using all water spectra. In the latter case, water spectra include samples collected at different geographic locations of a lake, different altitudes, and under various illumination conditions (e.g. sun glint). Samples

collected with visible lake bottom or aquatic vegetation (emergent, surface and below surface) were treated as invalid and excluded from the regression. The regression models with all samples were developed similar to Figs. 12–14, and provided in Table 2.

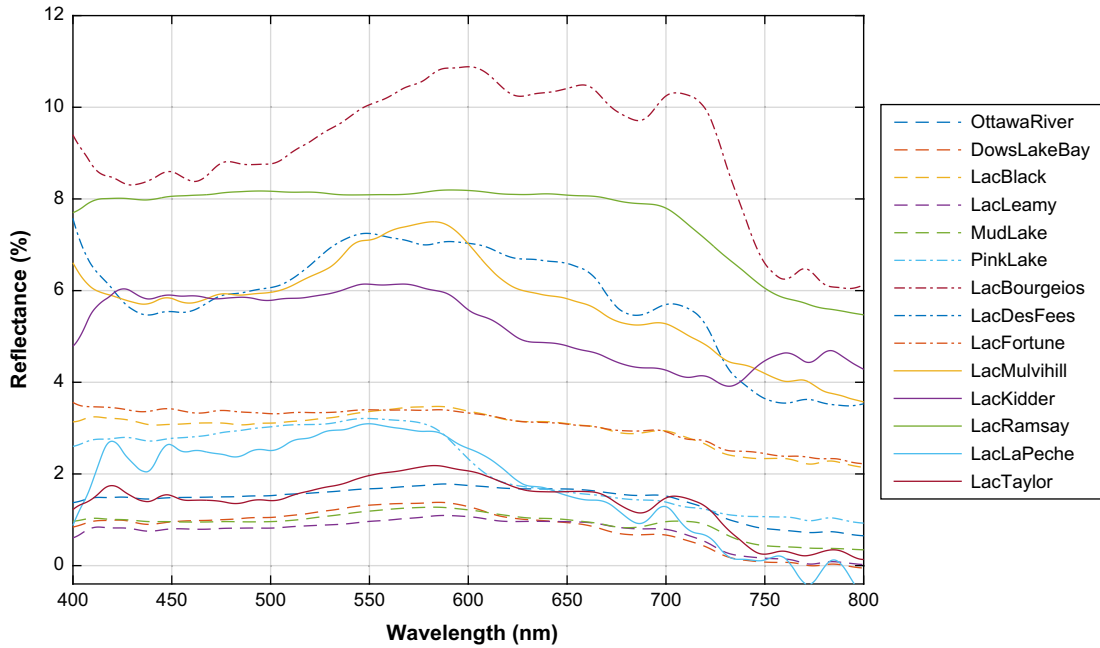


Fig. 11. Average spectra acquired by the UAV for each sampled water body. Spectra were acquired under sunny skies with minimal waves/sun glint, no vegetation, and no visible reflectance from the bottom of the water body. These averages were calculated from a range of 28–291 spectra samples for the given water bodies applying a 1D 10 nm moving window filter afterward.

Table 1
Average values for the measured parameters in each water body.

Site name	Date sampled	Number of spectra	Chl-a (µg/l)	CDOM (ppb)	Turbidity (FAU)
OttawaRiver	2016-05-25	77	5.69	20.05	NA ^a
DowsLakeBay	2016-05-30	28	6.20	19.16	12.3
LacBlack	2016-05-30	63	19.83	8.61	11.3
LacLeamy	2016-05-30	103	7.49	14.82	26.3
MudLake	2016-05-30	101	27.44	18.10	17.7
PinkLake	2016-05-30	63	3.36	5.11	5
LacBourgeois	2016-07-15	166	14.62	13.65	9.8
LacDesFees	2016-07-15	171	7.40	20.02	13.2
LacFortune	2016-07-15	271	11.51	17.21	7.6
LacMulvihill	2016-07-15	201	9.74	7.74	6.8
LacKidder	2016-07-29	291	2.35	13.22	5
LacRamsay	2016-07-29	241	4.45	2.88	8.2
LacLaPeche	2016-09-21	201	5.07	9.74	1.2
LacTaylor	2016-09-21	59	2.76	7.34	3.4

Note: Turbidity unit is Formazin Attenuation Unit (FAU), which measures the attenuation 180° to the incident beam using a near-infrared light source (USGS, 2013).
^a Turbidity data for the Ottawa River sample were not acquired.

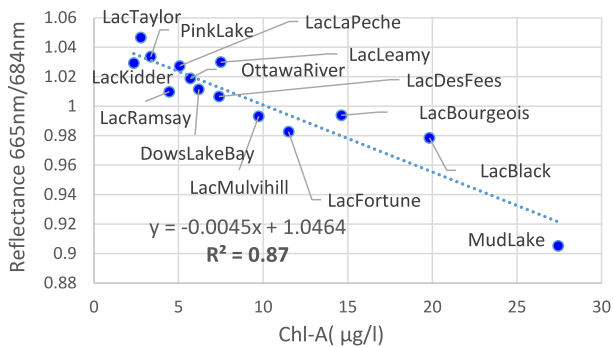


Fig. 12. Regression of Chl-a concentration against the ratio of reflectance at 665 nm and 684 nm.

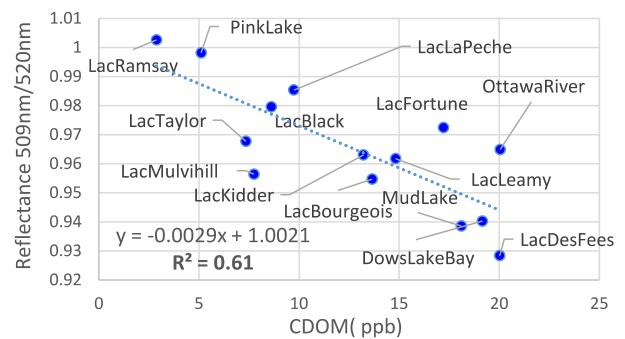


Fig. 13. Regression of CDOM concentration against the ratio of reflectance at 509 nm and 520 nm.

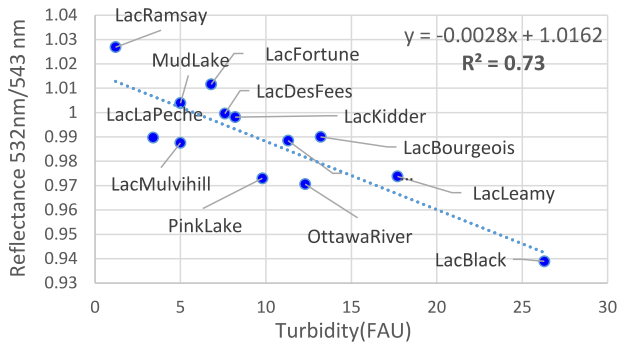


Fig. 14. Regression of Turbidity (FAU) against the ratio of reflectance at 532 nm and 543 nm.

According to Table 2, regression models with calm water spectra had higher R^2 compared with for all samples. The bands automatically chosen for band ratios were slightly shifted in wavelength, and the linear regression model coefficients changed by only small percentages. Chl-a was the most stable parameter to be modeled, with constant bands being chosen and with consistently high R^2 for all scenarios. The Turbidity model peak R^2 and selected bands were the same as for the calm water spectra model.

Based on the comparison of these two groups of water quality models, water spectra collected with all samples, including those acquired under less desirable conditions, can still maintain the model structure of calm water samples. For example, the band selection and regression coefficients were consistent with or without the less desirable water spectra. The R^2 of models, however, decreased when including samples of different environmental effects as given in Table 2. The reported model stability implies that, although sun glint can strongly affect water spectra in absolute terms, the effects on regression terms can be minimized by using band ratios, which is a typical strategy in water quality remote sensing.

These preliminary results will be applied in more in-depth water quality modelling research to develop capability for monitoring of the water bodies of this study and for broader research in other water applications (e.g. substrate analysis and mapping in shallow waters for habitat characterization and monitoring). The techniques can also be used in conjunction with future satellite hyperspectral sensors such as the HypSIIRI (Devred et al., 2013; Hestir et al., 2015) to aid in data calibration. Additional issues will require further research in order to fully exploit the advantages of UAV-based water-quality monitoring systems. In particular, the bidirectional reflectance distribution function (BRDF) of water reflectance makes it complicated to study water spectra at different sun angles and view angles. It is worth to fly the UAV at user-set angles, to explore the best practices of water data collection considering water BRDF issues. Furthermore, since sun glint is still a major source of error and cannot be avoided during data acquisition, new methods will be required to detect and

remove glint and its contributions to water spectra. These efforts should lead to further improvements in the predictive accuracy of hyperspectral water quality retrieval.

5. Summary and conclusions

This study presented results from the development and testing of a low-cost UAV-based reflectance spectra data collection platform for water quality information retrieval. A pair of low-cost and lightweight spectrometers (Ocean Optics STS-VIS) were used on the ground and on the UAV for measurement of downwelling irradiance and upwelling radiance, respectively. Following these setup, sources of potential spectral reflectance variability over water bodies were assessed. We found spectra averaging to be necessary in order to extract more reliable estimates of spectral reflectance from water bodies. Repeated sampling of deep water at a single location from one altitude (20 m) showed that a water spectra with average STD of 10.4% relative to the mean reflectance. Sampling at changing altitudes ranging between 20 m and 100 m produced an average STD of 2.9%, showing altitude within this range is not a factor affecting spectra variability. For data acquired over deep water at multiple locations, STD of spectra varied between 0.00011 and 0.0045, or 7.1% to 29.9% in relative terms. Collection of data over shallow water or where vegetation is present in the water column was also shown to alter reflectance, as expected. For example, analysis of deep to shallow water samples showed that reflectance increased by 20.2%, while presence of emergent aquatic plants changed the shape of the spectra to resemble reflectance of vegetation in the test site. Analysis of the substrate or aquatic vegetation conditions may, therefore, be another potential application for this system, but for water quality parameter estimation, spectral reflectance sampling should be done over locations that are free of aquatic vegetation, where depth is greater than the optical depth.

Assessment of other environmental factors showed that the strongest source of spectra variability was sun glint due to waves. Deep water without obvious waves and glint produced a STD of 2.8% of the average spectra, while water with waves and glint increased overall reflectance and STD (up to 9.3% of the average spectra). Further analyses of water surface and lighting conditions demonstrated that the impact of glint and shadow on water reflectance is complicated and there is no consistent trend observed between the proportion of glint in the spectrometer footprint and water reflectance. Such uncertainty may be caused by changes in the relative proportions of glint vs shadow in the images, as well as abrupt reflectance changes associated with incident angle and line-of-sight interactions due to waves.

The results of linear regression of water quality parameters based on a simple two-band ratio were encouraging, showing R^2 values of 0.87, 0.61, and 0.73 for Chlorophyll-a, CDOM, and Turbidity, respectively. The optimal ratios were similar to others in the literature as were the model R^2 values (Bierman et al., 2011; Matthews, 2011; Odermatt et al., 2012; Matsushita et al., 2015).

Table 2

The impact of environmental variables on the water quality parameter prediction.

Models	Water parameter	R^2	Equation [#]	b1 (nm)	b2 (nm)
Based on calm water samples (Figs. 12–14)	Chl-a	0.87	$y = -0.0045x + 1.0464$	665	684
	CDOM	0.61	$y = -0.0029x + 1.0021$	509	520
	Turbidity	0.73	$y = -0.0028x + 1.0162$	532	543
Based on all water samples	Chl-a	0.83	$y = -0.0045x + 1.0486$	665	684
	CDOM	0.49	$y = -0.0042x + 1.0135$	502	520
	Turbidity [†]	0.61	$y = -0.0018x + 1.0027$	533	543

Note: [#]In equations, x is the ratio of the two input bands' reflectance, as $x = \text{ref}(b1)/\text{ref}(b2)$, y is a water quality parameter (Chl-a, CDOM, or turbidity). [†]The highest R^2 of Turbidity model with all samples is 0.73 at band ratio of [626, 637] nm.

Leave-one-out cross-validation confirmed the consistency of the regression models on modelling water quality parameters. Comparison of water quality models using only calm water spectra and those with all valid water samples revealed similar band selection and regression parameters, but higher R^2 for the model based on calm water spectra. This result suggests that spectra collected under non-ideal lighting conditions (surface waves and sun glint) are still usable but will reduce the accuracy of regression models compared to models that are based on spectra collected under ideal lighting conditions.

Acknowledgments

This project was funded by a MITACS Accelerate grant (IT 056757) with contributions from NSERC Discovery Grants to M. Richardson and D. King. The authors would like to thank Mr. Stephen Bird from FSR Inc. for generous support and valuable discussion and Mr. Uzayr Siddiqui from DGES Carleton University for assistance in field work data collection. The authors thank the anonymous reviewers whose comments helped to improve this manuscript.

Appendix A. Spectrometer data quality

As an initial assessment of the spectrometer data quality, the dark noise of the Ocean Optics spectrometer was measured as a function of temperature because it was observed that the sensor became hot during operation. The spectrometer was placed in a hot environment until its exterior temperature reached 50 °C which is the highest allowed operational temperature. Then radiance spectra were measured at every 2 °C as it cooled until it reached room temperature. About 200 samples were acquired at

each temperature, each with an integration time of 0.3 s which is about the average integration time used for the water spectra as described.

The average dark noise spectrum measured using one of the Ocean Optics spectrometers at each temperature (every 2 °C) was tested, and the result showed that dark noise slightly increases with increasing temperature; an average increase of 1.6% occurred in recorded intensity from 28 °C to 50 °C. The noise increase is not consistent among bands: certain wavelengths had consistently lower noise for all temperatures (e.g. at about 600 nm), while others showed increased noise (e.g., at approximately 570 nm). The maximum standard deviation of intensity among bands was 3.85 at 28 °C, while that of 50 °C is 9.67, considering the average intensity was about 1510. These results show the impact of sensor warming on dark current noise is negligible, apart from the 700–800 nm range where water reflectance is close to zero and may therefore result in negative reflectance according to Eq. (1) (see Fig. A1).

Measurements of terrestrial targets were also made on the ground using both Ocean Optics spectrometers and an ASD Field-Spec Handheld spectrometer (25° FOV; 325–1075 nm range; 1.5 nm sampling interval). This analysis allowed comparison between two spectrometers of the same model and with another widely-used spectrometer model (the ASD Field-Spec) with known-reliability (Liu et al., 2014; Aasen et al., 2015). Under clear sunny conditions (12:30–14:00 May 11, 2016), five to ten samples were measured consecutively using each spectrometer viewing the same area of uniform lawn (short grass) and a homogenous concrete surface from a height of 0.5 m. The resulting spectral curves were compared for consistency in reflectance across the more limited wavelength range of the Ocean Optics sensors.

According to the measured spectra from the two Ocean Optics spectrometers (OO1, used for downwelling sun-sky irradiance;

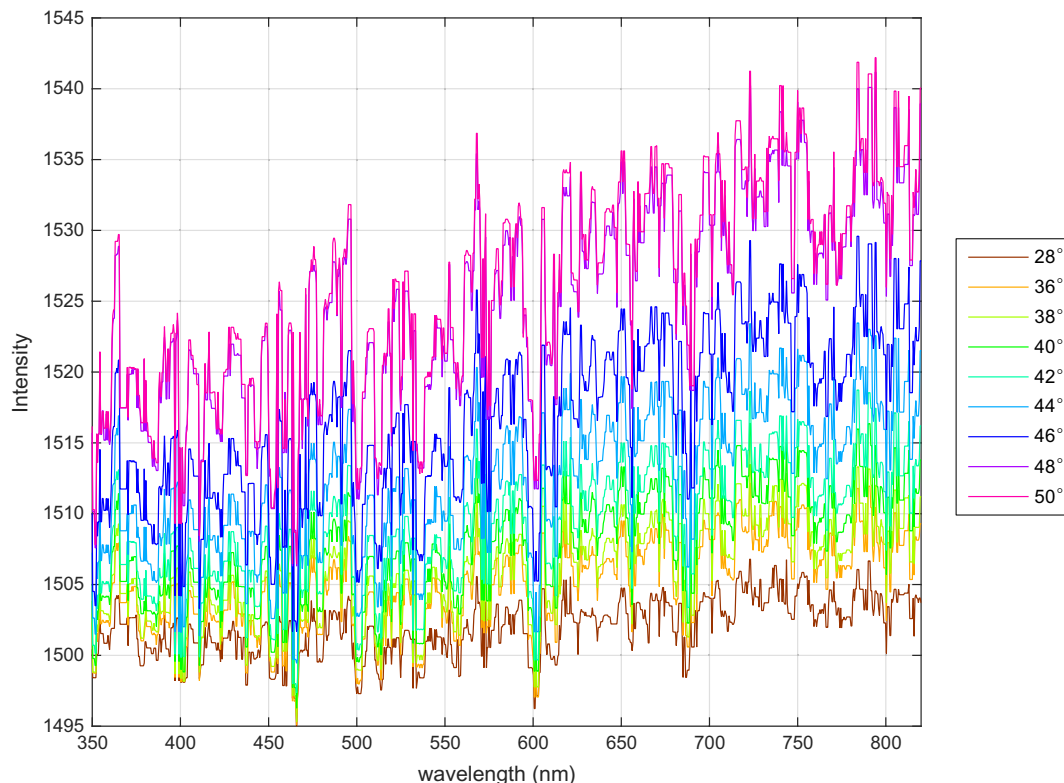


Fig. A1. Dark noise spectra (relative intensity) and their relation to sensor exterior temperature.

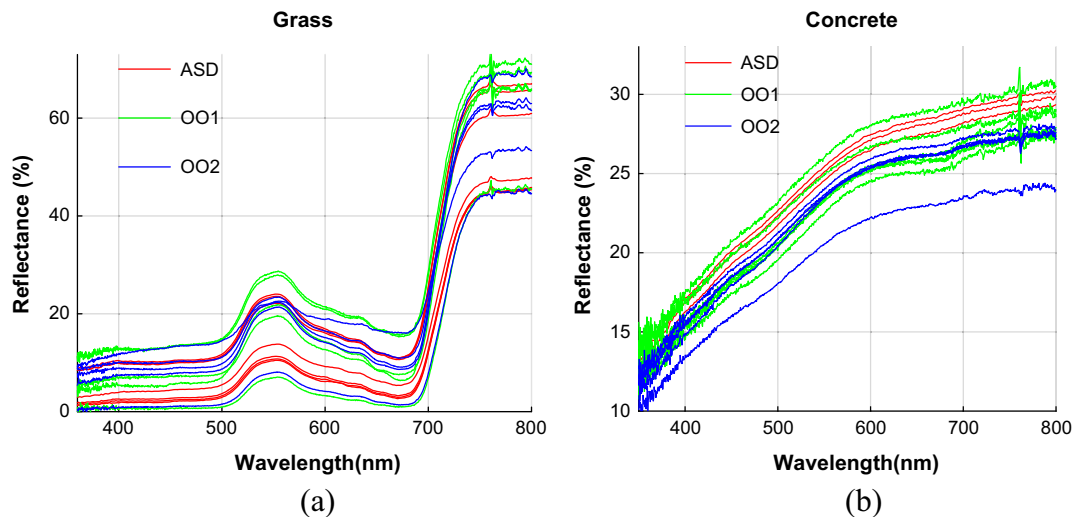


Fig. A2. Comparison of spectra measured using the ASD and two Ocean Optics (OO1, OO2) spectrometers for (a) grass; (b) concrete.

OO2, used in the UAV for surface reflectance) and the ASD spectrometer, the standard deviation of vegetation reflectance was 6.7%, 6.6%, 5.4% for the ASD, OO1, and OO2, respectively (see Fig. A2). Similar results for standard deviation were found from the concrete surface. This is an indicator of the precision that can be achieved with each of these spectrometers for such target types under typical operating conditions. There is increased noise below 400 nm and above 800 nm. Thus, the practical range of this spectrometer is from about 400 nm to 800 nm, which is sufficient for most water quality modelling.

References

- Aasen, H., Burkart, A., Bolten, A., Bareth, G., 2015. Generating 3D hyperspectral information with lightweight UAV snapshot cameras for vegetation monitoring: from camera calibration to quality assurance. *ISPRS J. Photogram. Remote Sens.* 108, 245–259.
- Ampe, E.M., Raymaekers, D., Hestir, E.L., Jansen, M., Knaeps, E., Batelaan, O., 2015. A wavelet-enhanced inversion method for water quality retrieval from high spectral resolution data for complex waters. *IEEE Trans. Geosci. Remote Sens.* 53 (2), 869–882.
- Ball, G.H., Hall, D.J., 1965. *Isodata, a Novel Method of Data Analysis and Pattern Classification*. Stanford Research Institute.
- Barr, D.R., Sherrill, E.T., 1999. Mean and variance of truncated normal distributions. *Am. Stat.* 53 (4), 357–361.
- Bergamino, N., Horion, S., Stenuite, S., Cornet, Y., Loiseau, S., Plisnier, P.D., Descy, J.P., 2010. Spatio-temporal dynamics of phytoplankton and primary production in Lake Tanganyika using a MODIS based bio-optical time series. *Remote Sens. Environ.* 114 (4), 772–780.
- Bierman, P., Lewis, M., Ostendorf, B., Tanner, J., 2011. A review of methods for analysing spatial and temporal patterns in coastal Water quality. *Ecol. Ind.* 11 (1), 103–114.
- Binding, C.E., Greenberg, T.A., Watson, S.B., Rastin, S., Gould, J., 2015. Long term water clarity changes in North America's Great Lakes from multi-sensor satellite observations. *Limnol. Oceanogr.* 60 (6), 1976–1995.
- Brezonik, P.L., Olmanson, L.G., Finlay, J.C., Bauer, M.E., 2015. Factors affecting the measurement of CDOM by remote sensing of optically complex inland waters. *Remote Sens. Environ.* 157, 199–215.
- Chen, J., Cui, T., Qiu, Z., Lin, C., 2014. A simple two-band semi-analytical model for retrieval of specific absorption coefficients in coastal waters. *ISPRS J. Photogram. Remote Sens.* 91, 85–97.
- Colomina, I., Molina, P., 2014. Unmanned aerial systems for photogrammetry and remote sensing: a review. *ISPRS J. Photogram. Remote Sens.* 92, 79–97.
- Cristianini, N., Hancock, J.M., Zvelebil, M.J., 2004. *Cross-Validation (K-Fold Cross-Validation, Leave-One-Out, Jackknife, Bootstrap)*, Dictionary of Bioinformatics and Computational Biology. John Wiley & Sons, Ltd.
- Devred, E., Turpie, K.R., Moses, W., Klemas, V.V., Moisan, T., Babin, M., Toro-Farmer, G., Forget, M.H., Jo, Y.H., 2013. Future retrievals of water column bio-optical properties using the hyperspectral infrared imager (hyspirci). *Remote Sens.* 5 (12), 6812–6837.
- Dörnhöfer, K., Oppelt, N., 2016. Remote sensing for lake research and monitoring – recent advances. *Ecol. Ind.* 64, 105–122.
- Gallegos, C.L., 2001. Calculating optical water quality targets to restore and protect submersed aquatic vegetation: overcoming problems in partitioning the diffuse attenuation coefficient for photosynthetically active radiation. *Estuaries* 24 (3), 381–397.
- Giardino, C., Kondratyev, K.Y., 1991. Optical models of mesotrophic and eutrophic water bodies. *Int. J. Remote Sens.* 12, 373–385.
- Gleason, A.C.R. et al., 2012. Detailed validation of the bidirectional effect in various case I and case II waters. *Opt. Express* 20 (7), 7630–7645.
- Hestir, E.L., Brando, V.E., Bresciani, M., Giardino, C., Matta, E., Villa, P., Dekker, A.G., 2015. Measuring freshwater aquatic ecosystems: the need for a hyperspectral global mapping satellite mission. *Remote Sens. Environ.* 167, 181–195.
- Knudby, A., Ahmad, S.K., Ilori, C., 2016. The potential for landsat-based bathymetry in Canada. *Can. J. Remote. Sens.* 42 (4), 367–378.
- Lee, Z., Carder, K.L., Mobley, C.D., Steward, R.G., Patch, J.S., 1999. Hyperspectral remote sensing for shallow waters: 2. Deriving bottom depths and water properties by optimization. *Appl. Opt.* 38 (18), 3831–3843.
- Lee, Z.P., Du, K.P., Arnone, R., 2005. A model for the diffuse attenuation coefficient of downwelling irradiance. *J. Geophys. Res. C: Oceans* 110 (2), 1–10.
- Liu, Y., Wang, T., Ma, L., Wang, N., 2014. Spectral calibration of hyperspectral data observed from a hyperspectrometer loaded on an unmanned aerial vehicle platform. *IEEE J. Select. Top. Appl. Earth Observat. Remote Sens.* 7 (6), 2630–2638.
- Matsushita, B., Yang, W., Yu, G., Oyama, Y., Yoshimura, K., Fukushima, T., 2015. A hybrid algorithm for estimating the chlorophyll-a concentration across different trophic states in Asian inland waters. *ISPRS J. Photogram. Remote Sens.* 102, 28–37.
- Matthews, M.W., 2011. A current review of empirical procedures of remote sensing in inland and near-coastal transitional waters. *Int. J. Remote Sens.* 32 (21), 6855–6899.
- McKee, D., Cunningham, A., Wright, D., Hay, L., 2007. Potential impacts of nonalgal materials on water-leaving Sun induced chlorophyll fluorescence signals in coastal waters. *Appl. Opt.* 46 (31), 7720–7729.
- Mobley, C.D., 1994. *Light and Water: Radiative Transfer in Natural Waters*. Academic Press, San Diego.
- Mobley, C.D., 1999. Estimation of the remote-sensing reflectance from above-surface measurements. *Appl. Opt.* 38 (36), 7442–7455.
- Moore, G.F., Aiken, J., Lavender, S.J., 1999. The atmospheric correction of water colour and the quantitative retrieval of suspended particulate matter in Case II waters: Application to MERIS. *Int. J. Remote Sens.* 20 (9), 1713–1733.
- Moore, T.S., Dowell, M.D., Bradt, S., Ruiz Verdu, A., 2014. An optical water type framework for selecting and blending retrievals from bio-optical algorithms in lakes and coastal waters. *Remote Sens. Environ.* 143, 97–111.
- Mouw, C.B., Greb, S., Aurin, D., DiGiacomo, P.M., Lee, Z., Twardowski, M., Binding, C., Hu, C., Ma, R., Moore, T., Moses, W., Craig, S.E., 2015. Aquatic color radiometry remote sensing of coastal and inland waters: challenges and recommendations for future satellite missions. *Remote Sens. Environ.* 160, 15–30.
- Odermatt, D., Gitelson, A., Brando, V.E., Schaepman, M., 2012. Review of constituent retrieval in optically deep and complex waters from satellite imagery. *Remote Sens. Environ.* 118, 116–126.
- Olmanson, L.G., Brezonik, P.L., Bauer, M.E., 2013. Airborne hyperspectral remote sensing to assess spatial distribution of water quality characteristics in large rivers: the Mississippi River and its tributaries in Minnesota. *Remote Sens. Environ.* 130, 254–265.
- Pajares, G., 2015. Overview and current status of remote sensing applications based on unmanned aerial vehicles (UAVs). *Photogram. Eng. Remote Sens.* 81 (4), 281–329.
- Palmer, S.C.J., Kutser, T., Hunter, P.D., 2015. Remote sensing of inland waters: challenges, progress and future directions. *Remote Sens. Environ.* 157, 1–8.

- Santer, R., Schmechtig, C., 2000. Adjacency effects on water surfaces: primary scattering approximation and sensitivity study. *Appl. Opt.* 39 (3), 361–375.
- Shuhaimi-Othman, M., Lim, E.C., Mushrifah, I., 2007. Water quality changes in Chini Lake, Pahang, West Malaysia. *Environ. Monit. Assess.* 131 (1–3), 279–292.
- Song, K., Ma, J., Wen, Z., Fang, C., Shang, Y., Zhao, Y., Wang, M., Du, J., 2017. Remote estimation of K_d (PAR) using MODIS and Landsat imagery for turbid inland waters in Northeast China. *ISPRS J. Photogram. Remote Sens.* 123, 159–172.
- USGS, 2013. Turbidity – Units of Measurement. from <<http://or.water.usgs.gov/grapher/fnu.html>>.
- Uto, K., Seki, H., Saito, G., Kosugi, Y., Komatsu, T., 2016. Development of a low-cost, lightweight hyperspectral imaging system based on a polygon mirror and compact spectrometers. *IEEE J. Select. Top. Appl. Earth Observat. Remote Sens.* 9 (2), 861–875.
- Vasilkov, A., Kopelevich, O., 1982. The reasons of maximum at about 700 nm on radiance spectra of the sea. *Oceanology* 22 (6), 945–950.
- Vertucci, F.A., Likens, G.E., 1989. Spectral reflectance and water quality of Adirondack mountain region lakes. *Limnol. Oceanogr.* 34 (8), 1656–1672.
- Wang, F., Han, L., Kung, H.T., van Arsdale, R.B., 2006. Applications of Landsat-5 TM imagery in assessing and mapping water quality in Reelfoot Lake, Tennessee. *Int. J. Remote Sens.* 27 (23), 5269–5283.
- Wang, L., Pu, H., Sun, D.W., 2016. Estimation of chlorophyll-a concentration of different seasons in outdoor ponds using hyperspectral imaging. *Talanta* 147, 422–429.
- Watanabe, F., Mishra, D.R., Astuti, I., Rodrigues, T., Alcântara, E., Imai, N.N., Barbosa, C., 2016. Parametrization and calibration of a quasi-analytical algorithm for tropical eutrophic waters. *ISPRS J. Photogram. Remote Sens.* 121, 28–47.
- Zarco-Tejada, P.J., González-Dugo, V., Berni, J.A.J., 2012. Fluorescence, temperature and narrow-band indices acquired from a UAV platform for water stress detection using a micro-hyperspectral imager and a thermal camera. *Remote Sens. Environ.* 117, 322–337.
- Zhang, Y., Liu, M., Qin, B., Feng, S., 2009. Photochemical degradation of chromophoric-dissolved organic matter exposed to simulated UV-B and natural solar radiation. *Hydrobiologia* 627 (1), 159–168.